

Determinations of ^{15}N Chemical Shift Anisotropy Magnitudes in a Uniformly ^{15}N , ^{13}C -Labeled Microcrystalline Protein by Three-Dimensional Magic-Angle Spinning Nuclear Magnetic Resonance Spectroscopy

Benjamin J. Wylie, W. Trent Franks, and Chad M. Rienstra*

Department of Chemistry, Department of Biochemistry, and Center for Biophysics and Computational Biology, University of Illinois at Urbana–Champaign, 600 South Mathews Avenue, Urbana, Illinois 61801

Received: January 24, 2006; In Final Form: March 29, 2006

Amide ^{15}N chemical shift anisotropy (CSA) tensors provide quantitative insight into protein structure and dynamics. Experimental determinations of ^{15}N CSA tensors in biologically relevant molecules have typically been performed by NMR relaxation studies in solution, goniometric analysis of single-crystal spectra, or slow magic-angle spinning (MAS) NMR experiments of microcrystalline samples. Here we present measurements of ^{15}N CSA tensor magnitudes in a protein of known structure by three-dimensional MAS solid-state NMR. Isotropic ^{15}N , $^{13}\text{C}\alpha$, and $^{13}\text{C}'$ chemical shifts in two dimensions resolve site-specific backbone amide recoupled CSA line shapes in the third dimension. Application of the experiments to the 56-residue β 1 immunoglobulin binding domain of protein G (GB1) enabled 91 independent determinations of ^{15}N tensors at 51 of the 55 backbone amide sites, for which ^{15}N – $^{13}\text{C}\alpha$ and/or ^{15}N – $^{13}\text{C}'$ cross-peaks were resolved in the two-dimensional experiment. For 37 ^{15}N signals, both intra- and interresidue correlations were resolved, enabling direct comparison of two experimental data sets to enhance measurement precision. Systematic variations between β -sheet and α -helix residues are observed; the average value for the anisotropy parameter, δ ($\delta = \delta_{zz} - \delta_{\text{iso}}$), for α -helical residues is 6 ppm greater than that for the β -sheet residues. The results show a variation in δ of ^{15}N amide backbone sites between -77 and -115 ppm, with an average value of -103.5 ppm. Some sites (e.g., G41) display smaller anisotropy due to backbone dynamics. In contrast, we observe an unusually large ^{15}N tensor for K50, a residue that has an atypical, positive value for the backbone ϕ torsion angle. To our knowledge, this is the most complete experimental analysis of ^{15}N CSA magnitude to date in a solid protein. The availability of previous high-resolution crystal and solution NMR structures, as well as detailed solid-state NMR studies, will enhance the value of these measurements as a benchmark for the development of ab initio calculations of amide ^{15}N shielding tensor magnitudes.

Introduction

The magnetic shielding is a fundamental property in NMR spectroscopy. The isotropic chemical shifts derived from this shielding are the single most frequently measured NMR parameters in studies of molecular structure and bonding.^{1–3} A thorough understanding of the origins of the chemical shift can be leveraged in a variety of ways to improve chemical analysis, including structure, bonding, and dynamics. For example, Paul and Grant first observed the γ -gauche effect, where the chemical shift depended strongly upon the conformation of hydrocarbons.⁴ Similar effects were later identified in other organic molecules, including early solid-state NMR (SSNMR) studies of peptides that demonstrated variations in $^{13}\text{C}\alpha$ and $^{13}\text{C}\beta$ shifts as a function of conformation.^{5–8} Spera and Bax subsequently demonstrated the trend in $^{13}\text{C}\alpha$ and $^{13}\text{C}\beta$ isotropic shifts specifically as a function of secondary structure in proteins.⁹ Over the past decade these trends have been systematically analyzed and extended to $^{13}\text{C}'$, amide ^{15}N , and nearby ^1H sites; the resulting empirical databases of backbone and partial side-chain ^{15}N and ^{13}C chemical shifts have been utilized to generate predictive and structure refinement tools, including the chemical shift index (CSI)^{10,11} and TALOS,^{9,12} which are applicable to

proteins in both solution and the solid state.¹³ These observations led to a variety of chemical-shift-driven geometry optimization routines.^{14–18} State-of-the-art methods demonstrate excellent semiempirical agreement for $^{13}\text{C}\alpha$ and $^{13}\text{C}\beta$ shifts in proteins,^{19,20} useful for high-resolution structural refinement^{21,22} once appropriate adjustments are made to ensure accurate referencing.^{20,23} Nevertheless, the isotropic chemical shifts typically observed in solution NMR report only a portion of the structural information inherent to the full chemical shift tensor. Measurements of the individual chemical shift anisotropy (CSA) tensor elements are therefore expected to improve structural precision accordingly.

In particular, the peptide backbone amide ^{15}N CSA tensor exquisitely relates electronic structure to NMR observables. Amide ^{15}N sites display a large (~ 40 ppm) dispersion of isotropic chemical shifts, which depend on amino acid type, primary structure (neighboring residues), secondary structure, side-chain conformation, hydrogen bonding, and other electrostatic effects.^{2,24–26} Together these diverse effects contribute to the difficulty of accurately calculating ^{15}N CSA values from ab initio quantum mechanical theory.^{2,3,25–29} However, the detailed sensitivity on local structural parameters also implies that with the appropriate experimental tensor databases as training sets it will be possible to develop more accurate and efficient computational approaches to describe these effects. This

* Author to whom correspondence should be addressed. E-mail: rienstra@scs.uiuc.edu.

is a prerequisite to predicting tensors accurately, a capability that would contribute substantially to structure determination and refinement methodology.

Experimental studies of isotropic ¹⁵N chemical shifts and relaxation parameters are numerous in both the solution and the solid-state NMR communities, because of the ease and cost-effectiveness of ¹⁵N labeling in a variety of growth media. Two-dimensional (2D) ¹H–¹⁵N correlation experiments such as heteronuclear single quantum coherence (HSQC),^{30,31} heteronuclear multiple quantum coherence (HMQC),³² and transverse relaxation-optimized spectroscopy (TROSY)^{33–35} are the most often employed experiments in modern solution NMR, providing especially high sensitivity for studies of high-molecular-weight protein complexes, small volumes, and high-throughput structure–activity relationship screening techniques.^{36,37} These common solution NMR techniques will benefit from an improved understanding of the ¹⁵N CSA tensor. For example, the TROSY experiment relies upon cross-correlated relaxation effects and destructive interference between the ¹H–¹⁵N dipole vector and the principal elements of the amide ¹⁵N chemical shift tensor. The optimal enhancement of sensitivity and resolution as a function of magnetic field strength (*B*₀) is observed when the magnitude of the amide ¹H–¹⁵N dipolar coupling is equal to the projection of the ¹⁵N tensor along the ¹H–¹⁵N axis. Therefore the resolution, sensitivity, and field dependence of TROSY spectra rely directly on ¹⁵N CSA parameters, including the tensor magnitude, asymmetry, and orientation.

Unraveling the relationships of the several contributions to the full chemical shift tensor is also crucial for accurate analysis of relaxation data often used to describe protein dynamics.^{38–43} Much of the dynamics information derived from solution NMR relates directly or indirectly to amide ¹⁵N and ¹H measurements, whose precise interpretation in turn relies upon known CSA values. The most utilized dynamic probes in solution NMR are the ¹⁵N and ¹H *T*₁ and *T*₂ values.^{38–43} Both the design of experiments and the interpretation of resulting data will be aided greatly by accurate knowledge of the ¹⁵N CSA tensor. A thorough understanding of the ¹⁵N CSA and its relationship to fundamental electronic structure will therefore enable greater information content to be extracted from relatively simple data sets as well as determination of optimal experimental conditions.

In the solid state, measurements of ¹⁵N tensors and ¹H–¹⁵N dipole vectors relative to lipid bilayers provide a powerful combined methodology for membrane protein structure determination by the polarization inversion spin exchange at magic angles (PISEMA) family of techniques.^{44–46} Recent applications of PISEMA have increasingly relied upon analysis of the dipolar coupling information, in the form of dipolar waves,^{47–49} to constrain peptide structure in the bilayer.⁵⁰ In part this development has arisen from the less precise knowledge of ¹⁵N tensor magnitude and orientation, which translates to greater structural uncertainty. Therefore the accuracy of the analysis of 2D PISEMA spectra in the form of polarity index slant angle (PISA) wheels could be further improved by detailed knowledge about how amide tensor sites vary as a function of secondary structure and electrostatic environment.

A final application of improved ¹⁵N CSA information will be the enhanced prediction of isotropic amide ¹⁵N chemical shifts for proteins of known (or postulated) structure. Accurate prediction and interpretation of isotropic chemical shift spectra as a function of chemical environment holds promise as a high-throughput technique for structure determination in several contexts. Isotropic chemical shift prediction programs perform well in cases where conformational effects dominate the

observed changes; however, such programs demonstrate relatively poor performance in cases where competing effects, including electrostatics, also contribute significantly to the isotropic shifts. For example, SHIFTX¹⁹ correlation coefficients between experimental and predicted isotropic chemical shifts are 0.980 for ¹³Cα sites, which are dominated primarily by backbone conformation, and 0.996 for ¹³Cβ sites, where electrostatic contributions are generally even less substantial. For ¹³C′ and ¹⁵N, the correlations are 0.863 and 0.909, respectively, indicating the greater challenge of predicting these sites, where not only conformation but also hydrogen bonding play significant roles. In the case of amide ¹⁵N sites, the root-mean-square (RMS) error was 2.43 ppm, the largest of all chemical shift classes studied, owing to the contribution of the many effects mentioned above.

All of these applications will be enhanced by expanded databases of experimental CSAs, determined with high accuracy and precision. So far, most efforts to measure ¹⁵N CSA values in proteins have relied upon solution NMR cross-correlated relaxation and/or residual dipolar and CSA measurements in partially aligned media.^{38,51–59} These solution NMR techniques often require multiple alignment media to constrain the tensor orientation unambiguously. Despite major advances in these techniques over the past decade, it remains experimentally challenging to determine overall tensor magnitudes with high certainty because the residual effect is a small (typically 0.1–1.0%) percentage of the tensor magnitude, and therefore measurement precision of a tenth of a hertz or better is essential. Even in cases where well-optimized experiments have given high-precision, unambiguous data, comparisons to other experimental techniques will be valuable, especially since SSNMR methods offer enhanced potential for identifying unambiguous orientations with respect to a molecular frame of reference. SSNMR measurements also enable more direct comparisons to crystal structures, to explain differences that sometimes arise between solution NMR and crystal structures.

Due to the inherent value of the ¹⁵N CSA and the difficulty of its accurate measurement in solution NMR, a number of studies in recent years have aimed to determine ¹⁵N tensors in solid peptides and proteins.^{60–70} Experimental determination of ¹⁵N chemical shift tensors in solids has historically been restricted to small peptides, including goniometric studies of single crystals,^{60,61,68,70} Herzfeld–Berger⁷¹ analysis of sideband manifolds,⁶⁹ or static spectra.^{69,72} Notable among these studies is a frequently cited single-crystal analysis of the ¹⁵N chemical shift tensor of glycyl glycine hydrochloride, revealing the ¹⁵N tensor had a *δ* value of −100.3 ppm and exhibited near axial symmetry.⁶¹ These values have been used as a starting point for many subsequent studies, including measurements of capped glycine dipeptides that revealed greater deviations from axial symmetry, larger spans, and an orientation of the N–C′ dipole to the *z*-axis of the CSA tensor near 96°. ^{62–64} Experimental studies of residues with larger side chains are not as abundant, in large part because the approaches used are not generally applicable to high-field MAS studies of uniformly ¹⁵N,¹³C-labeled biomacromolecules.

In this work, we contribute a substantial number of new amide ¹⁵N tensor magnitude measurements to the experimental database, with the first systematic three-dimensional (3D) measurements of this type in a well-structured microcrystalline protein, the β1 immunoglobulin binding domain of protein G (GB1). We have previously shown that the isotropic chemical shifts and empirically predicted backbone torsion angles of GB1 agree well with both the solution NMR structure and the reported

crystal structures; we also have reported ^{13}C CSAs that give further insight into backbone and side-chain conformation.^{73,74} Here we extend this work to ^{15}N measurements. Using several ^{15}N isotropic chemical shifts that are resolved in the one-dimensional (1D) cross polarization magic-angle spinning (CP-MAS) spectrum at the 750 MHz ^1H frequency, we have compared the traditional method of analysis, slow magic-angle spinning Herzfeld–Berger analysis,⁷¹ with the recently introduced recoupling of chemical shift anisotropy (ROCSA) method;⁷⁵ for those sites, we find agreement within the statistical error of the two experiments. Subsequently, we proceeded to perform two 3D experiments, which resolve the large majority of ^{15}N sites throughout the protein. In the first 3D experiment, the amide ($\text{N}[i]$) CSA tensor and isotropic chemical shift were correlated to the intrasidue $^{13}\text{C}\alpha[i]$ isotropic shift; the $\text{N}[i]$ – $\text{C}\alpha[i]$ 2D provided sufficient resolution to analyze 44 ^{15}N CSA tensors. In the second experiment, the amide ($\text{N}[i]$) CSA tensor and isotropic chemical shift were correlated to the preceding carbonyl $\text{C}'[i-1]$ isotropic shift; likewise, 47 backbone ^{15}N CSA tensors were extracted from this experiment. The two 3D experimental data sets together provided ^{15}N tensor measurements for 51 of the 55 backbone ^{15}N amide resonances. The combination of the two experiments enabled a complementary analysis of relative dipolar orientation effects for peptide amide sites, to confirm that the orientation of the ^{15}N CSA tensor relative to the local dipolar vectors did not significantly perturb the interpretation. Therefore systematic errors in the analysis were avoided, and the combined results give high confidence in the tensor magnitude. Although the determination of the asymmetry by this method is significantly less precise, the experimental determinations of tensor magnitude will complement the ongoing theoretical studies in this discipline and contribute to an improved fundamental understanding of the ^{15}N chemical shift tensor, benefiting the aforementioned applied studies of protein structure and dynamics.

Experimental Methods

Sample Preparation. The T2Q mutant of GB1 was prepared as described previously.⁷³ For the ^{15}N – ^{13}C -based 3D experiments, ~22 mg of hydrated microcrystalline $\text{U-}^{15}\text{N}$, ^{13}C GB1 was packed into the central 80% of the volume of a thin-wall 3.2 mm rotor (34 μL , Varian, Inc., Palo Alto, CA). Approximately two-thirds of this material was protein (~15 mg or 2.5 μmol), as determined by the signal intensities observed in ^{13}C and ^{15}N spectra with equilibrium polarization, in comparison to microcrystalline, anhydrous model compounds of known quantity. A second sample $\text{U-}^{15}\text{N}$ GB1 (~12 mg or 2 μmol) was packed into a standard 3.2 mm rotor for one-dimensional slow-spinning spectra at high field. In addition, $\text{U-}^{15}\text{N}$, ^{13}C *N*-acetyl valine was prepared by established methods, diluted to 20% concentration in natural abundance material, and packed into the full length of a standard 3.2 mm rotor.

NMR Spectroscopy. The ^{15}N – ^{13}C 3D experiments were executed at 11.7 T (499.86 MHz ^1H , 125.7 MHz ^{13}C , and 50.6 MHz ^{15}N Larmor frequencies) using an InfinityPlus spectrometer (Varian, Inc., Palo Alto, CA) with a 3.2 mm T3 Balun probe optimized for ^1H – ^{13}C – ^{15}N operation. This probe design offers high B_1 homogeneity (>90% in the region of the sample coil used here), critical for optimal precision in the ROCSA dimension, providing a minimal spread in the B_1 -dependent scaling factors and minimizing signal loss under such multiple pulse recoupling sequences. The MAS rate was 11.111 kHz, maintained to ± 2 Hz (90.0 μs rotor period).

The ROCSA recoupling sequence⁷⁶ was combined with SPECIFIC CP⁷⁷ to generate a 3D ^{15}N – ^{15}N – ^{13}C experiment

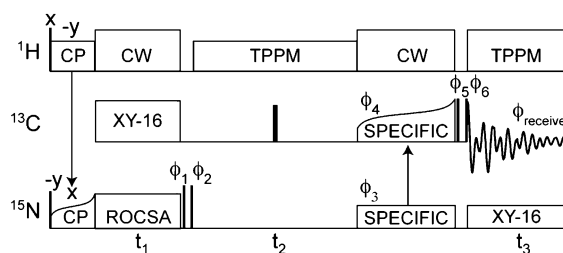


Figure 1. Pulse sequence diagram of ^{15}N – ^{15}N – ^{13}C 3D ROCSA. The ROCSA element was inserted before the indirect ^{15}N chemical shift evolution period of a ^{15}N – ^{13}C 2D experiment. ROCSA was applied under CW decoupling on ^1H (~120 kHz) and rotor-synchronized XY π -pulse decoupling on ^{13}C . An eight-step phase cycle was used: $\phi_1 = (-y, -y, -y, -y, -y, -y, -y, -y)$, $\phi_2 = (y, y, -x, -x, -y, -y, x, x)$, $\phi_3 = (x, -x, y, -y, -x, x, -y, y)$, $\phi_4 = (x, x, -x, -x, x, x, -x, -x)$, $\phi_5 = (-y, -y, y, y, -y, -y, y, y)$, $\phi_6 = (x, x, y, y, -x, -x, -y, -y)$, $\phi_{\text{receiver}} = (x, -x, y, -y, -x, x, -y, y)$. Hypercomplex sampling was achieved in the t_1 (ROCSA) dimension by adding the States–TPPI phase to ϕ_1 . The TPPI phase list was added to ϕ_3 to provide quadrature detection in t_2 .

analogous to our previously published 3D ^{13}C – ^{13}C – ^{13}C experiment,⁷⁴ where the nucleus in square brackets denotes the site at which the CSA line shape was measured. As illustrated in Figure 1, ^{15}N magnetization was created by ramped cross polarization (CP) from ^1H . The ROCSA pulse sequence was then applied under continuous wave (CW) decoupling on ^1H (~120 kHz) and π pulse XY-16 decoupling on ^{13}C , where the π pulses each had a pulse width of 5 μs . The ROCSA period is followed by a z -filter, to select the desired coherence transfer pathway. Phase cycling of these pulses acts as a filter for coherences that have evolved according to the ROCSA Hamiltonian in t_1 . ROCSA is followed by an isotropic ^{15}N chemical shift evolution period and SPECIFIC CP, transferring polarization from ^{15}N – $^{13}\text{C}\alpha$ or ^{15}N – $^{13}\text{C}'$.^{77,78} We found the optimal transfer efficiency for ^{15}N – $^{13}\text{C}'$ when $\omega\text{N} = 5/2\omega\text{R}$ and $\omega\text{C} = 7/2\omega\text{R}$ and the optimal ^{15}N – $^{13}\text{C}\alpha$ transfer near the condition $\omega\text{N} = 5/2\omega\text{R}$ and $\omega\text{C} = 3/2\omega\text{R}$, where ωN and ωC refer to the nutation frequencies on ^{15}N and ^{13}C , respectively, and ωR to the magic-angle spinning rate. The field on the ^{13}C channel had a tangent ramp of approximately ± 2 kHz. Two-pulse phase modulation (TPPM) decoupling was utilized during acquisition,⁷⁹ with a field of ~75 kHz, a 15° total phase shift, and 6.5 μs pulse width. The ^{15}N – $^{13}\text{C}'$ SPECIFIC CP efficiency was approximately 55%, enabling efficient signal averaging with 24 scans per row; in practice this was executed by performing the entire experiment three times, each with eight scans per row. Comparison of individual 3D data sets (prior to coaddition) demonstrated spectrometer stability to within better than 1% of the peak signal intensity, over the acquisition time of tens of hours to several days. The ^{15}N – $^{13}\text{C}\alpha$ -based experiment was signal-averaged for 32 scans per row (four sets of eight scans per row), to compensate for the lower efficiency (~40%) of the ^{15}N – $^{13}\text{C}\alpha$ polarization transfer. The pulse delay was 2 s. Each row, in the direct dimension, was comprised of 8192 points with a dwell of 5 μs , giving a total acquisition time of 40.96 ms per row. The 128 real points were acquired in the ^{15}N dimension, with a dwell of 180 μs (23 ms maximum evolution time in t_1). The 48 points in the ROCSA dimension were acquired with hypercomplex States–time proportional phase increment (States–TPPI) sampling (24 hypercomplex points), with a dwell of 90 μs (one rotor period). Therefore the total measurement time for the 3D N – C' experiment was ~86 h and for the N – $\text{C}\alpha$ experiment was 115 h.

The form of ROCSA used here was a windowless version, where the parameters a and b were set to 0 and 0.5, respectively,

instead of the original values of 0.0239 and 0.467.⁷⁶ This version of the pulse sequence has the advantages of eliminating isotropic chemical shift evolution and providing total suppression of ± 1 and ± 2 Fourier components of the homonuclear dipolar coupling. The drawback of this approach is that the line shape is slightly distorted from the static powder pattern because the scaling factors for the ± 1 and ± 2 Fourier components of the CSA tensor are no longer equal. Nevertheless, this effect is easily simulated, so it does not fundamentally alter the ability to extract CSA information from the experimental data. The scaling factors for the Fourier coefficients in this version of ROCSA are

$$\chi_{\pm 1}^{\text{CSA}} = 0.2218 \quad \chi_{\pm 2}^{\text{CSA}} = 0.3001 \quad (1)$$

As a control to confirm the accuracy of the ¹⁵N ROCSA measurements, in addition to the two- and three-dimensional ROCSA spectra, slow-spinning ¹⁵N 1D spectra were acquired, and the sidebands of four resolved ¹⁵N peaks were analyzed. These ¹⁵N 1D spectra were acquired at the 749.7 MHz ¹H frequency (17.6 T, 76.00 MHz ¹⁵N Larmor Frequency) using a Varian INOVA console with a Varian 3.2 mm Balun narrow-bore ¹H–¹³C–¹⁵N triple resonance probe. Three ¹⁵N 1D spectra were acquired, at spinning rates of $12\,500 \pm 5$, 3850 ± 3 , and 2550 ± 3 Hz.

NMR Data Processing. Slow-spinning ¹⁵N CP-MAS data were processed using NMRPipe.⁸⁰ The fast MAS spectrum and two slow-spinning spectra were processed with 10 Hz of Gaussian line broadening, and the integrated sideband intensities for four baseline-resolved peaks (T11, G14, T49, and F52) were extracted using the peak-picking utilities provided with NMRPipe (pk.tcl). These sidebands were then fit in Mathematica using the “mPackages” Mathematica macros and subroutines and the MAS_sb_analysis_v2 notebook provided by Malcolm Levitt and co-workers (<http://www.mhl.soton.ac.uk/public/software/mPackages/>). This fitting procedure reports both a “best fit” and a 68.3% confidence interval for the two-parameter fit (anisotropy and asymmetry).

The 3D [¹⁵N]–¹⁵N–¹³C experiment was processed using NMRPipe.⁸⁰ A Lorentzian-to-Gaussian apodization function was employed in the two isotropic chemical shift dimensions, with a net line broadening of 30 Hz for ¹³C and 5 Hz for ¹⁵N. Each region of the ¹⁵N–¹³C 2D plane (F2, F3) was analyzed independently by modeling each peak as a Gaussian and integrating peak intensities, using the chemical shift assignments determined previously;⁷³ in the samples specifically used for experiments here, chemical shifts were found to be in agreement within ± 0.1 ppm with the previously published values, with no systematic differences. Each plane provided peak intensities for the ROCSA time-domain (t_1) trajectories corresponding to each resolved site. The trajectories were extracted using the autoFit.tcl package provided with NMRPipe. No apodization function was applied to this ROCSA dimension. The trajectory from each extracted peak was then fit as described further below.

Recoupled CSA Line Shape Fitting. In this work we employ the Haebleren Convention⁸¹ to describe the chemical shift tensor. Like the other conventions in common use, there are three axes in the principal axis system (PAS) corresponding to the three inflection points in a static powder pattern. They are defined as δ_{xx} , δ_{yy} , and δ_{zz} . They are ordered according to the relation

$$|\delta_{zz} - \delta_{\text{iso}}| \geq |\delta_{xx} - \delta_{\text{iso}}| \geq |\delta_{yy} - \delta_{\text{iso}}| \quad (2)$$

This ordering corresponds to their magnitude in the “traceless representation”, in which the chemical shift tensor is decom-

posed into its zeroth order component, the isotropic chemical shift, δ_{iso} ($\delta_{\text{iso}} = 1/3(\delta_{xx} + \delta_{yy} + \delta_{zz})$), and the traceless chemical shift anisotropy tensor, where the axes are often indicated with a single letter subscript as δ_x , δ_y , and δ_z to distinguish them from the axes of the full tensor. While these elements are of great importance in Cartesian space, for efficient mathematical manipulation of these tensor values in a Fourier series in the basis of irreducible spherical tensors, Haebleren introduced the anisotropy parameter, δ ($\delta = \delta_{zz} - \delta_{\text{iso}} = \delta_z$) (sometimes called the “reduced anisotropy”), and the asymmetry parameter, η ($\eta = (\delta_{yy} - \delta_{xx})/(\delta_{zz} - \delta_{\text{iso}}) = (\delta_y - \delta_x)/\delta$). In this context the nonzero elements of the irreducible spherical tensor operators corresponding to the chemical shift in the PAS are

$$\rho_{00} = \delta_{\text{iso}} \quad \rho_{20} = \sqrt{\frac{3}{2}} \delta \quad \rho_{2\pm 2} = \frac{1}{2} \eta \delta \quad (3)$$

In addition, he defined the “chemical shift anisotropy”, $\Delta\delta = 3/2\delta = \delta_{zz} - 1/2(\delta_{xx} + \delta_{yy})$. It should be noted for clarity that in the original formulation of this convention the subscripted symbol “ σ ” was used instead of “ δ ” for individual elements of the chemical shift tensor and the chemical shift anisotropy, which could also be used interchangeably for elements of the chemical shielding tensor. To emphasize the distinction between the chemical shift and chemical shielding and avoid any confusion with standard notation for the standard deviation, we have opted to use the symbol “ δ ” with the appropriate subscripts for elements of the chemical shift tensor and an unsubscripted “ δ ” to designate the anisotropy parameter, in keeping with Haebleren’s original convention.

Therefore in all numerical simulations, we modeled ROCSA line shapes in terms of three parameters: (1) the anisotropy parameter, δ ; (2) the asymmetry, η ; (3) a phenomenological single-exponential relaxation rate, Γ_1 . In the version of the pulse sequence used in this study, the isotropic chemical shift is averaged to zero, eliminating the need to fit this as an additional adjustable parameter or assume a nonzero value based on other measurements. Line shapes were fit first to a library of SIMPSON⁸² simulations, with initial guesses for the parameters based on visual inspection of the spectra. Near this set of parameters, the values of δ were incremented by 0.25 ppm, η by 0.025, and relaxation as an analytical single-exponential decay in the time domain (applied to the time-domain trajectories outside of SIMPSON in increments of 25 Hz). This approach provided initial fits of the line shapes but required approximately 3 central processing unit (CPU) minutes per simulation, limiting the numerical precision of the grid search. Moreover, to address the concern that the choice of initial conditions might bias the fitting procedure, we developed a more rigorous and efficient Fortran program to perform the statistical analysis using a finer grid of simulations (i.e., with smaller increments in the values of the adjustable parameters). The program assumed the ROCSA average Hamiltonian theory (AHT)⁸³ result and included a phenomenological single-exponential relaxation, i.e., a constant rate of decay for all coherences.^{84–87} The two simulation methods agreed quantitatively in the assumed limit of ideal B_1 homogeneity, but the customized Fortran code enabled statistical analysis to be performed 2–3 orders of magnitude faster than in SIMPSON. This routine was essential to find the optimal agreement between experimental and simulated spectra for the entire set of >100 line shapes and to analyze the statistical distributions rigorously with Monte Carlo analysis in a computationally feasible time frame (i.e., tens of hours to a few days with a small cluster of Linux workstations). In the AHT simulation library, δ was incremented by 0.2 ppm, η by 0.01,

and Γ_1 by 250 s^{-1} . The simulations were performed with powder averaging over large three-angle Lebedev Euler angle sets.⁸⁸ Typically, 24 780 sets of α , β , and γ converge to smooth, simulated powder patterns even in the absence of relaxation. Individual simulations with this size powder set could be generated in a few seconds each on standard workstations with $\sim 2\text{ GHz}$ Athlon or PowerPC processors; comparable SIMPSON simulations required several minutes. In practice, large libraries were generated using a cluster of several Athlon nodes running overnight calculations; the best fit and statistical analysis was then performed by searching against this library on the order of 1000 times, to create a statistically significant number of Monte Carlo results.

The experimental data was compared to the simulation library in the time domain, with the best fit determined to be the minimal value for the root-mean-square deviation (RMSD) between trajectories. In addition to the parameters noted above (δ , η , and Γ_1), a fourth adjustable parameter was used to account for the variations in intensity of the first data point in the ROCSA trajectory. This amplitude scaling factor was close but not exactly equal to unity; it accounts for the fact that under multiple pulse sequences a fraction of the polarization is almost immediately lost due to the effects of phase transients and B_1 inhomogeneity. This effect manifests itself as a baseline error in the frequency domain of ROCSA line shapes acquired under conditions of poor B_1 homogeneity. For example, a subset of experiments was performed on a probe with a 4 mm unbalanced solenoid resonator (500 MHz ^1H frequency); the poor B_1 homogeneity in this case led to amplitude scaling factors of ~ 0.5 (corresponding to a loss of approximately half of the total polarization within the first rotor period of ROCSA irradiation); these experiments were not pursued further. In the data acquired with the 3.2 mm Balun probe, this correction factor was typically 0.9–0.95, corresponding to a loss of only 5–10% of the signal during the first rotor period of the ROCSA sequence. (The correction factor is approximately equal to the percentage of ^{13}C signal observed upon a 450° pulse, relative to the 90° pulse.) Therefore a total of four adjustable parameters were utilized to fit 48 experimental data points. The relaxation rate, Γ_1 , was typically $1000\text{--}2000\text{ s}^{-1}$ and showed no obvious systematic trends due, for example, to chemical shift offsets or protonation state of the neighboring ^{13}C sites.

A Monte Carlo algorithm was implemented to determine standard errors. After finding the best-fit spectrum, the standard deviation was calculated using the bootstrapping method,⁸⁹ where Gaussian random noise is added to the spectrum, weighted by the RMSD between the spectrum and the best-fit simulation. The standard deviation, σ , for the anisotropy parameter, δ , typically was in the range of 1–4 ppm; we denote this as $\sigma(\delta)$. For a single parameter fit, by convention σ reports the 68.3% confidence interval. However, because the error bars presented here are for a four-parameter fit of 48 experimental data points, the true 68.3% confidence interval is a multiple of σ depending upon the covariance of the fit parameters, typically $1.0\sigma\text{--}3.0\sigma$. We therefore assumed a conservative interpretation of the data and report 68.3% confidence intervals at $\pm 2.0\sigma$, the upper bound observed in independent Monte Carlo analysis of the line shapes that we observed.

Results and Discussion

Two-Dimensional Experiments in *N*-Acetyl Valine. The ^{15}N ROCSA pulse sequence and analysis procedures were first tested on a model peptide that mimics valine in a β -sheet conformation, *N*-acetyl valine (NAV). The ROCSA line shape

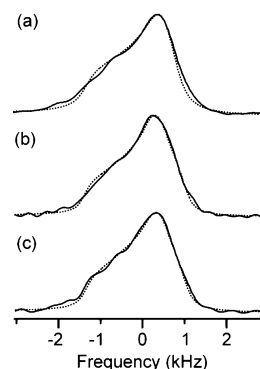


Figure 2. Experimental ^{15}N ROCSA line shapes determined from three types of experiments for the amide ^{15}N of NAV. In all cases 128 transients were acquired, with a 2.0 s recycle delay. (a) Line shape from a 2D ROCSA experiment, correlating isotropic and anisotropic chemical shifts. The isotropic ^{15}N dimension was processed with 15 Hz Gaussian apodization; the signal-to-noise ratio (SNR) of the first point in the trajectory was ~ 80 . Tensor values were determined to be $\delta = -107.5 \pm 5.1\text{ ppm}$ and $\eta = 0.28 \pm 0.16$. (b) Line shape from a 2D experiment, where the ^{15}N ROCSA signal is detected on the ^{13}C channel following SPECIFIC CP to the $\text{C}\alpha$ nucleus. The isotropic ^{13}C dimension was processed with 25 Hz Gaussian apodization. The SNR of the first point in the trajectory was ~ 154 . Tensor values were determined to be $\delta = -107.0 \pm 4.0\text{ ppm}$ and $\eta = 0.45 \pm 0.13$. (c) Line shape from a 2D experiment, where the ^{15}N ROCSA signal is detected on the ^{13}C channel following SPECIFIC cross polarization to the $\text{C}\alpha$ nucleus. The isotropic ^{13}C dimension was processed with 25 Hz Gaussian apodization. The SNR of the first point in the trajectory was 143. Tensor values were determined to be $\delta = -106.0 \pm 4.1\text{ ppm}$ and $\eta = 0.44 \pm 0.12$. In all cases the experimental data are shown as solid lines and the simulated data as dotted lines.

of NAV was measured at 11.111 kHz. The ^{15}N nutation frequency was set to 44.4 kHz to satisfy the requirement that $\omega_{\text{rf}} = 4\tau_r$ for this version of the ROCSA experiment employing the $\text{C}3_3^1$ symmetry element. The measurement was performed with three different versions of the pulse sequence to assess potential systematic errors. The first version was the standard 2D ROCSA pulse sequence with ROCSA directly following $^1\text{H}\text{--}^{15}\text{N}$ CP and detection on the ^{15}N channel immediately following the z -filter. The second version incorporated SPECIFIC CP as illustrated in Figure 1, transferring the polarization band selectively from the ^{15}N to the $^{13}\text{C}\alpha$ site for detection. In the third version, polarization transfer from the ^{15}N to the directly bonded acetyl $^{13}\text{C}'$ preceded ^{13}C detection. In both ^{13}C -detected versions of the experiment, it was unnecessary to frequency-label the indirect isotropic chemical shift dimension, since NAV has only one ^{15}N site. Therefore the 2D experiment with ^{13}C detection was equivalent to the 3D experiment to be performed on proteins. The three spectra (Figure 2) demonstrate the precision with which δ can be determined but also reveal subtle differences that may arise from different polarization transfer pathways. Each pseudo-static line shape has approximately the same appearance, and each fits to a comparable value of δ (within the respective measurement error). The ^{15}N -detected version fits to $-107.5 \pm 5.1\text{ ppm}$, the $^{15}\text{N}\text{--}^{13}\text{C}\alpha$ version fits to $-107.0 \pm 4.0\text{ ppm}$, and the $^{15}\text{N}\text{--}^{13}\text{C}'$ version fits to $-106.0 \pm 4.1\text{ ppm}$. These values agree well with previous determinations, most recently by Hong, who found that $\delta = -106\text{ ppm}$ and $\eta = 0.27$.⁷² In our study η tended to be larger, especially when measured in the experiments including a $^{15}\text{N}\text{--}^{13}\text{C}$ CP transfer. The ^{15}N -detected line shape fit to an asymmetry of 0.28 ± 0.16 , the $^{15}\text{N}\text{--}^{13}\text{C}\alpha$ to 0.45 ± 0.13 , and the $^{15}\text{N}\text{--}^{13}\text{C}'$ to 0.44 ± 0.12 .

To understand the origin of these variations in η , we analyzed the statistical covariance among δ , η , and Γ_1 . The fitted value

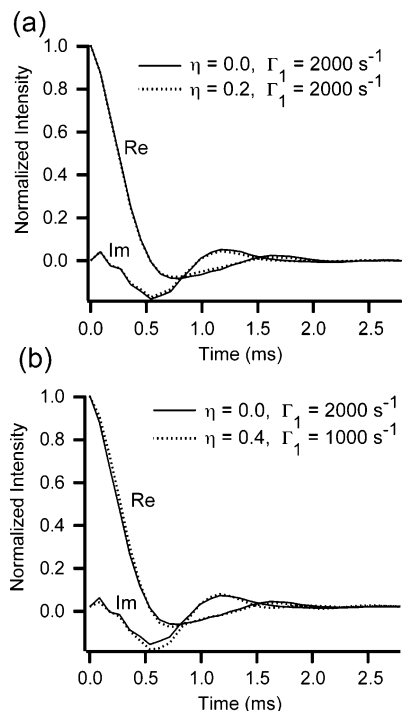


Figure 3. Illustration of the covariance between relaxation and asymmetry fit parameters. (a) Time-domain simulations of two trajectories with the same Γ_1 value but different values of η . The RMSD between the trajectories is 0.5%. This level of noise would mask approximately a difference of 0.2 in η . (b) Time-domain simulations of two spectra with varying η and Γ_1 . The RMSD between these two data sets is 1.0%, but the variation in η is 30%, with a 50% variation in relaxation.

for δ varied little as the other parameters were adjusted, consistent with the fact that the edges of the spectra are essentially invariant with η and Γ_1 . However, a significantly larger covariance between η and Γ_1 was observed, reflecting the fact that line broadening in the ROCSA dimension can move the apparent position of the singularity indicative of σ_{yy} , the element of the tensor closest to δ_{iso} . Figure 3a illustrates how relaxation on the order of 2000 s^{-1} (the best fit value for all NAV spectra) can obscure differences between η values in this range of near axial symmetry ($\eta < 0.4$). For example, in Figure 4, a line shape with $\eta = 0.0$ and $\Gamma_1 = 2000 \text{ s}^{-1}$ was generated as a test trajectory; this simulation was then fit to a library of simulations, assuming different Γ_1 values. The result is a family of line shapes that are nearly identical, with relaxation masking the true asymmetry (Figure 4). The variation in η ranges from 0.0 to 0.4 depending upon the assumed relaxation value. We conclude that ROCSA, in its current implementation, has a relatively poor ability to distinguish among asymmetry parameters less than 0.5; the random uncertainty in the sense is similar to the Herzfeld–Berger method, but in addition there may be a systematic tendency in the ROCSA experiments toward larger asymmetry parameter values. This systematic error may possibly be exacerbated by the orientation dependence of the ^{15}N – ^{13}C polarization transfer. Qualitatively similar variations relative to single-crystal tensor values appear in the previously published ^{13}C spectra of NAV.⁷⁶ Our analysis suggests that methods less sensitive to relaxation, such as constant time implementations of ROCSA and/or improved decoupling methods during the multiple pulse sequence, may enable improved precision and accuracy in the fitting of the asymmetry parameter. More detailed analysis of the relative orientation of the CSA to dipolar tensors in these data sets might also improve the determination of η . We reserve further analysis of this problem for future work

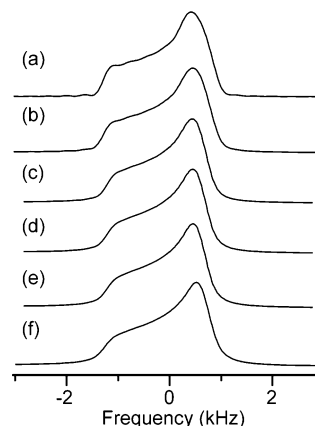


Figure 4. Simulations of line shapes with same value of the anisotropy parameter (δ) but with varying values of the asymmetry parameter (η) and relaxation rate (Γ_1). The RMSD relative to a reference simulation with $\eta = 0.0$, $\Gamma_1 = 2000 \text{ s}^{-1}$, and $\delta = -100 \text{ ppm}$ is reported. In the subsequent fits, Γ_1 and δ were fixed to the reported value, and η was adjusted to minimize the RMSD value. (a) $\eta = 0.35$, $\Gamma_1 = 500 \text{ s}^{-1}$, RMSD = 2.7%; (b) $\eta = 0.30$, $\Gamma_1 = 1000 \text{ s}^{-1}$, RMSD = 1.7%; (c) $\eta = 0.22$, $\Gamma_1 = 1500 \text{ s}^{-1}$, RMSD = 0.8%; (d) $\eta = 0.16$, $\Gamma_1 = 1750 \text{ s}^{-1}$, RMSD = 0.4%; (e) $\eta = 0.10$, $\Gamma_1 = 1900 \text{ s}^{-1}$, RMSD = 0.2%; (f) the reference simulated spectrum, $\eta = 0.0$, $\Gamma_1 = 2000 \text{ s}^{-1}$, RMSD = 0% (by definition). While the RMSD over this group of line shapes does not exceed 2.7%, the value of η ranges from 0.0 to 0.35. Typical best-fit RMSD values for experiments in this study range from 1.8% to 4.5%.

and focus in the remainder of this study on measurements of the tensor magnitude, which is fit with substantially greater accuracy and precision than η .

Herzfeld–Berger Analysis of GB1 Select Amide ^{15}N Sites. Slow magic-angle spinning spectra of uniformly ^{15}N -labeled GB1 were acquired at 17.6 T at spinning speeds of 2550 and 3850 Hz and compared to an isotropic spectrum acquired at $\omega_R/2\pi = 12.5 \text{ kHz}$ (Figure 5). GB1 has especially good resolution for a solid protein, with four amide (T11, G14, T49, and F52) as well as several amino ^{15}N signals resolved in the 1D spectrum. These signals have been assigned in previous work based upon 2D ^{15}N – ^{13}C and ^{13}C – ^{13}C and 3D ^{15}N – ^{13}C – ^{13}C and ^{13}C – ^{15}N – ^{13}C correlation spectra.⁷³ Peak intensities of center bands and sidebands were determined by integration and used as input parameters for the Herzfeld–Berger analysis program (Experimental Methods). The values for δ determined by Herzfeld–Berger analysis (Table 1) agree well with our experimental results for the ROCSA 3D experiments on the protein GB1.

In all cases, the values for δ and η agree within the uncertainties of the two experiments. It is well-known that Herzfeld–Berger analysis accuracy can be improved by acquiring several data sets over a range of spinning rates, in particular very slow spinning rates where several sideband orders would be observed. Unfortunately, spectra at slower MAS rates in a uniformly ^{15}N -labeled protein result in overlap of first-order sidebands with center bands from other peaks, even in the case of GB1, which has especially high resolution. It is possible to incorporate TOSS^{90,91} into a 2D isotropic–anisotropic correlation experiment; however, this method still requires resolution in a single isotropic ^{15}N dimension and is not compatible with uniform ^{15}N , ^{13}C labeling, in which the ^{13}C – ^{15}N dipolar coupling magnitude (0.9–1.4 kHz) is within an order of magnitude of the ^{15}N CSA magnitude, at the fields available to this study ($\sim 5 \text{ kHz}$ at 11.7 T and $\sim 7.5 \text{ kHz}$ at 17.55 T). Therefore the Herzfeld–Berger analysis was performed with a ^{15}N -labeled GB1 sample to avoid the complications of ^{13}C – ^{15}N couplings.

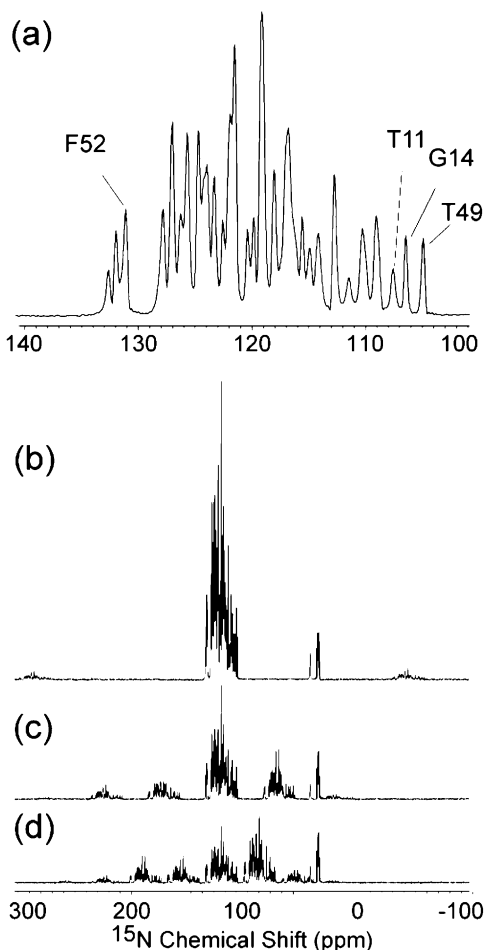


Figure 5. ^{15}N 1D spectra at slow MAS and a 750 MHz ^1H frequency. All spectra (512 scans) were processed with 10 Hz Gaussian apodization and normalized to the same absolute scale. (a) Amide region of the ^{15}N 1D spectrum at 12.5 kHz MAS, illustrating several resolved sites as labeled. F52 is partially overlapped with D40, but its intensities could be accurately extracted by modeling as Lorentzian line shapes. The four resolved sites were fit by Herzfeld–Berger⁷¹ analysis, as reported in Table 1. (b) Full spectrum at a 12.5 kHz MAS rate, illustrating the relatively weak first-order sidebands of the amide resonances. (c) ^{15}N 1D spectrum at 3850 Hz MAS. Five manifolds are resolved (center band and ± 2 sidebands). (d) ^{15}N 1D spectrum at a 2550 Hz MAS rate. Seven manifolds are resolved (center band and ± 3 sidebands).

TABLE 1: Comparison of Herzfeld–Berger⁷¹ Sideband Analysis with ROCSA Recoupling for Resolved ^{15}N Sites in GB1^a

| residue | Herzfeld–Berger | | ROCSA | |
|---------|----------------------|-----------------|----------------------|-----------------|
| | δ | η | δ | η |
| T11 | -101.1 ± 5.0 ppm | 0.14 ± 0.14 | -104.0 ± 2.1 ppm | 0.36 ± 0.09 |
| G14 | -100.2 ± 3.0 ppm | 0.27 ± 0.10 | -99.8 ± 4.0 ppm | 0.38 ± 0.09 |
| T49 | -102.3 ± 3.0 ppm | 0.15 ± 0.15 | -100.9 ± 2.0 ppm | 0.36 ± 0.04 |
| F52 | -98.5 ± 3.0 ppm | 0.17 ± 0.17 | -101.7 ± 3.1 ppm | 0.37 ± 0.08 |

^a The values for the asymmetry parameter η determined by ROCSA are systematically larger than those found in Herzfeld–Berger experiments. As discussed in the text, this is likely due to a shortcoming of the ROCSA experiment, which contributes a systematic error in addition to the random (statistical) error reported here.

Furthermore we found that it was beneficial to perform the Herzfeld–Berger analysis at the highest magnetic field available to us; similar spectra acquired at the 500 MHz ^1H frequency were significantly less accurate. The ROCSA experiment, in contrast, was optimally implemented at 500 MHz where high decoupling powers ($\omega_{\text{H}}/2\pi \approx 120$ kHz) and ^{15}N excitation ($\omega_{\text{N}}/2\pi \approx 50$ kHz) could be more easily achieved.

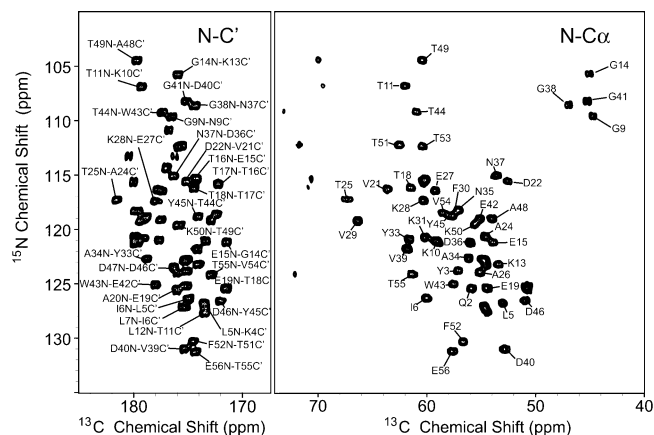


Figure 6. (a) First ^{15}N – ^{13}C plane of the ^{15}N – ^{13}C 3D experiment. The spectrum was acquired with 128 points (180 μs dwell) in the indirect ^{15}N dimension and 8192 points (5 μs dwell) in the direct ^{13}C dimension, with 24 scans per row resulting in a total measurement time of ~ 1.8 h. The spectrum processed with 5 and 30 Hz Gaussian line broadening in the ^{15}N and ^{13}C dimensions, respectively. A subset of resonance assignments is illustrated; complete resonance assignments were previously published.⁷³ The average SNR is 110:1. (b) First ^{15}N – ^{13}C plane of the ^{15}N – $^{13}\text{C}\alpha$ 3D experiment. Acquisition parameters are the same as in part a but with 32 scans per row resulting in a total measurement time of 2.4 h. The spectrum is processed with 5 and 30 Hz Gaussian line broadening in the ^{15}N and ^{13}C dimensions, respectively. The average SNR is 40:1, owing to the greater line width of the $^{13}\text{C}\alpha$ resonances and the lower efficiency of ^{15}N – $^{13}\text{C}\alpha$ transfer relative to ^{15}N – ^{13}C .

ROCSA Analysis of GB1 Amide Sites. The first 2D ^{15}N – ^{13}C planes of the 3D ROCSA experiment performed on GB1 are shown in Figure 6. The spectra, processed with 30 Hz of net Gaussian apodization in the ^{13}C dimension reveal resolution of most sites in each 2D plane as well as fine structure arising from ^{13}C – ^{13}C scalar couplings (one-bond couplings of ~ 55 Hz between C' and $\text{C}\alpha$ and ~ 35 Hz between $\text{C}\alpha$ and $\text{C}\beta$). The 2D planes each uniquely resolve approximately 50 unique backbone sites in GB1. In general, the sites that may be overlapped in one 2D plane tend to be well-resolved in the other. Therefore almost all of the backbone sites (51 out of 55 amides) could be analyzed without resorting to four-dimensional (4D) experiments (three dimensions of isotropic shifts and one dimension of ROCSA). Rather, we could use the third dimension to measure line shapes, as shown in Figure 7. This enabled an especially thorough analysis of the line shapes throughout the protein, including sites of differing secondary structure, within common data sets.

The values of δ and η measured here (Table 2) show that the anisotropy parameter values determined from the ^{15}N – $^{13}\text{C}'$ and ^{15}N – $^{13}\text{C}\alpha$ data sets agree within the experimental error.

The plot of δ versus residue number (Figure 8) displays a trend of increasing values for δ in the α -helix and near-helical turn conformations.

In the α -helix the average value of δ is -106.2 ± 2.3 ppm, while in the β -sheets the average δ is -100.5 ± 2.4 ppm (Table 3). Our observation is consistent with observations from solution cross-correlation and relaxation measurements^{51,55,56,59} as well as measurements of tripeptides in the solid state.^{69,70} However, our measurements show a slightly larger variation (5.7%) than those in the studies of Bax and co-workers (4%).⁵⁶ We surmised that part of this difference may have arisen from the orientation dependence of the dipolar transfer, since we observed larger changes in line shapes as a function of the polarization transfer pathway (N – C' versus N – $\text{C}\alpha$) in helical residues, although the orientation dependence using adiabatic tangent ramped ^{15}N –

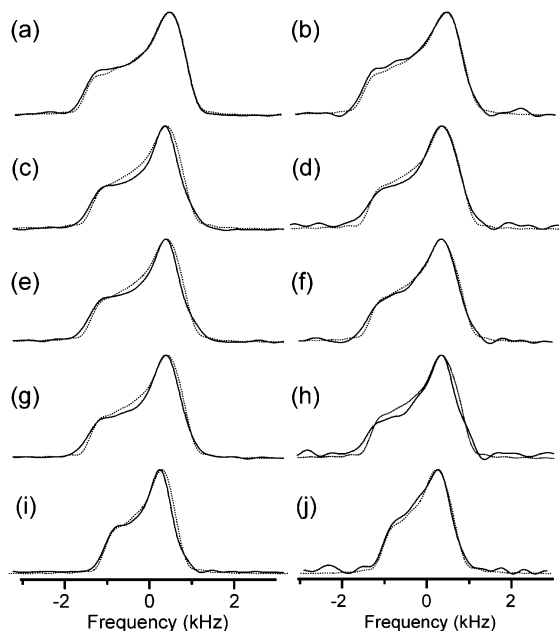


Figure 7. Pairs of ¹⁵N ROCSA pseudo-static powder patterns extracted from 3D experiments. Each pair of line shapes corresponds to the same ¹⁵N amide backbone tensor, extracted from sites resolved in both N–Cα and N–C' spectra. The values of the anisotropy parameter, δ , range from -116.1 to -74.8 ppm. The left column is composed of line shapes from the N–C' experiment, and the right column is composed of line shapes for the same resonance, measured from the N–Cα. The peaks and fit values are: (a) K50 N–C', $\delta = -115.1 \pm 1.5$ ppm, $\eta = 0.32 \pm 0.03$; (b) K50 N–Cα, $\delta = -116.1 \pm 3.4$ ppm, $\eta = 0.34 \pm 0.07$; (c) Y3 N–C', $\delta = -100.8 \pm 4.7$ ppm, $\eta = 0.36 \pm 0.11$; (d) Y3 N–Cα, $\delta = -101.0 \pm 4.6$ ppm, $\eta = 0.40 \pm 0.07$; (e) K13 N–C', $\delta = -99.2 \pm 5.3$ ppm, $\eta = 0.36 \pm 0.08$; (f) K13 N–Cα, $\delta = -100.6 \pm 4.0$ ppm, $\eta = 0.36 \pm 0.08$; (g) N35 N–C', $\delta = -103.8 \pm 4.0$ ppm, $\eta = 0.36 \pm 0.08$; (h) N35 N–Cα, $\delta = -103.8 \pm 7.3$ ppm, $\eta = 0.42 \pm 0.13$; (i) G41 N–C', $\delta = -74.8 \pm 3.0$ ppm, $\eta = 0.40 \pm 0.07$; (j) G41 N–Cα, $\delta = -81.2 \pm 3.5$ ppm, $\eta = 0.40 \pm 0.06$.

¹³C CP should be reduced in comparison to nonadiabatic sequences. We tested this hypothesis by using previously published values for the amide tensor orientations.^{62–64} Modeling the transfer with a simple trigonometric function (as discussed previously)⁹² improved the fit quality by approximately 0.5% RMSD. However, the inclusion of this orientation dependence did not alter the other fit parameters (δ , η) to a significant extent. Therefore the orientation dependence alone does not appear to account for the greater disparity observed in anisotropy between helical and sheet residues.

A second possible explanation for this difference is backbone dynamics. The variation of anisotropy parameters from one residue to another has been reported by several studies of NMR relaxation on ¹⁵N-labeled proteins, including ubiquitin and ribonuclease H,^{51,55,56,58,59} with reported values ranging from -77 to -154 ppm, with a mean value of -112 ppm (although solution NMR relaxation studies have typically reported this in terms of the larger quantity $\Delta\delta = 3/2\delta$). The average magnitude of δ reported in our study is approximately 10% smaller (-103 ppm). As discussed previously,^{56,70} CSA parameters measured in the solution state tend to be slightly larger than those measured in the solid state, because of corrections made in the solution data for local backbone motion; i.e., the solution CSA value is scaled according to the ¹H–¹⁵N order parameter as determined from other experiments. In our studies of GB1 in the solid state, we observed a modest trend (Figure 8 of Franks et al.⁷³) in which the effective ¹H–¹⁵N bond length among helical residues was slightly shorter than the rest of the protein

TABLE 2: Amide ¹⁵N CSA Tensor Values in GB1 Determined in This Study^a

| residue | N–C'-based experiment | | | | N–Cα-based experiment | | | |
|---------|-----------------------|------------------------|--------|----------------------|-----------------------|----------------------|--------|----------------------|
| | δ (ppm) | 2σ (δ) | η | 2σ (η) | δ (ppm) | 2σ (η) | η | 2σ (η) |
| M1 | NA | | | | NA | | | |
| Q2 | NA | | | | -103.4 | 5.9 | 0.42 | 0.10 |
| Y3 | -100.8 | 4.7 | 0.36 | 0.11 | -101.0 | 4.6 | 0.40 | 0.07 |
| K4 | NA | | | | NA | | | |
| L5 | -101.4 | 4.2 | 0.36 | 0.08 | -103.8 | 3.1 | 0.38 | 0.05 |
| I6 | -98.8 | 4.0 | 0.38 | 0.08 | -103.2 | 5.2 | 0.42 | 0.08 |
| L7 | -96.4 | 5.1 | 0.36 | 0.14 | NA | | | |
| N8 | -95.8 | 3.6 | 0.38 | 0.07 | NA | | | |
| G9 | -102.6 | 3.2 | 0.38 | 0.06 | -102.0 | 7.0 | 0.34 | 0.20 |
| K10 | NA | | | | NA | | | |
| T11 | -103.8 | 2.5 | 0.36 | 0.04 | -104.4 | 3.8 | 0.36 | 0.06 |
| L12 | -104.4 | 2.3 | 0.34 | 0.05 | NA | | | |
| K13 | -99.2 | 5.3 | 0.38 | 0.12 | -100.6 | 4.0 | 0.36 | 0.08 |
| G14 | -95.2 | 5.9 | 0.36 | 0.14 | -103.8 | 5.4 | 0.40 | 0.11 |
| E15 | -104.0 | 4.2 | 0.40 | 0.08 | -104.4 | 4.2 | 0.42 | 0.06 |
| T16 | -101.6 | 4.4 | 0.38 | 0.08 | NA | | | |
| T17 | -98.8 | 3.6 | 0.38 | 0.07 | NA | | | |
| T18 | -99.0 | 3.9 | 0.36 | 0.09 | -95.6 | 9.1 | 0.49 | 0.05 |
| E19 | -99.8 | 4.6 | 0.38 | 0.11 | -101.4 | 4.8 | 0.44 | 0.07 |
| A20 | -98.6 | 3.0 | 0.34 | 0.07 | NA | | | |
| V21 | -98.2 | 3.8 | 0.38 | 0.07 | -97.6 | 6.0 | 0.40 | 0.09 |
| D22 | -104.6 | 3.6 | 0.38 | 0.06 | -108.7 | 5.0 | 0.36 | 0.09 |
| A23 | NA | | | | NA | | | |
| A24 | NA | | | | -108.7 | 5.4 | 0.46 | 0.07 |
| T25 | -107.9 | 3.6 | 0.38 | 0.05 | -105.2 | 5.6 | 0.42 | 0.08 |
| A26 | -102.4 | 4.4 | 0.38 | 0.10 | -107.7 | 6.2 | 0.48 | 0.08 |
| E27 | -107.1 | 4.1 | 0.36 | 0.08 | -102.8 | 4.6 | 0.38 | 0.09 |
| K28 | -105.1 | 4.4 | 0.36 | 0.08 | -103.0 | 4.7 | 0.42 | 0.10 |
| V29 | -106.3 | 3.1 | 0.38 | 0.06 | -102.6 | 3.9 | 0.42 | 0.08 |
| F30 | -105.9 | 4.5 | 0.34 | 0.09 | -103.6 | 3.5 | 0.40 | 0.06 |
| K31 | NA | | | | -108.5 | 5.2 | 0.42 | 0.06 |
| Q32 | NA | | | | NA | | | |
| Y33 | -107.5 | 3.5 | 0.38 | 0.07 | -104.4 | 5.6 | 0.44 | 0.09 |
| A34 | -111.9 | 3.5 | 0.34 | 0.07 | -108.9 | 5.4 | 0.40 | 0.09 |
| N35 | -103.8 | 4.0 | 0.36 | 0.08 | -103.8 | 7.3 | 0.42 | 0.12 |
| D36 | NA | | | | -106.1 | 5.1 | 0.42 | 0.09 |
| N37 | -99.8 | 2.7 | 0.46 | 0.04 | -101.4 | 3.5 | 0.46 | 0.05 |
| G38 | -111.9 | 1.7 | 0.32 | 0.04 | -108.1 | 4.2 | 0.38 | 0.07 |
| V39 | -107.9 | 3.0 | 0.32 | 0.06 | -109.5 | 4.1 | 0.34 | 0.08 |
| D40 | -94.8 | 2.6 | 0.34 | 0.05 | -96.6 | 3.1 | 0.36 | 0.06 |
| G41 | -74.8 | 2.9 | 0.40 | 0.07 | -81.2 | 3.4 | 0.40 | 0.06 |
| E42 | -97.4 | 5.1 | 0.40 | 0.11 | -99.4 | 5.2 | 0.46 | 0.07 |
| W43 | -98.1 | 3.8 | 0.44 | 0.07 | -102.2 | 5.2 | 0.44 | 0.07 |
| T44 | -96.6 | 5.1 | 0.40 | 0.11 | -96.2 | 6.2 | 0.48 | 0.06 |
| Y45 | -99.6 | 3.9 | 0.38 | 0.08 | NA | | | |
| D46 | -101.2 | 3.4 | 0.36 | 0.08 | -105.6 | 4.8 | 0.40 | 0.08 |
| D47 | -90.7 | 6.0 | 0.38 | 0.17 | NA | | | |
| A48 | -109.9 | 3.0 | 0.38 | 0.05 | -108.5 | 4.7 | 0.42 | 0.07 |
| T49 | -100.4 | 2.2 | 0.36 | 0.04 | -103.0 | 4.8 | 0.34 | 0.09 |
| K50 | -115.1 | 1.7 | 0.32 | 0.03 | -116.1 | 3.4 | 0.34 | 0.07 |
| T51 | NA | | | | -101.2 | 4.8 | 0.42 | 0.07 |
| F52 | -100.8 | 3.9 | 0.36 | 0.08 | -103.2 | 4.9 | 0.38 | 0.08 |
| T53 | NA | | | | -100.2 | 5.4 | 0.44 | 0.08 |
| V54 | -104.8 | 5.2 | 0.40 | 0.10 | -104.8 | 6.4 | 0.38 | 0.11 |
| T55 | -100.0 | 5.1 | 0.40 | 0.10 | -101.6 | 5.2 | 0.38 | 0.10 |
| E56 | -98.6 | 4.2 | 0.36 | 0.08 | -100.8 | 4.4 | 0.38 | 0.06 |

^a The values for the asymmetry parameter η are systematically larger than those found in Herzfeld–Berger experiments. As discussed in the text, this is likely due to a shortcoming of the ROCSA experiment, which contributes a systematic error in addition to the random (statistical) error reported here. Therefore the absolute value of the asymmetry parameters is likely to be unreliable for the purpose of quantum chemical calculations.

(i.e., the observed dipolar coupling was larger). Therefore, if we were to apply a correction in which the reported ¹⁵N tensor is the experimentally determined tensor divided by the ¹H–¹⁵N coupling, then our β -sheet values would on average increase throughout the protein. This correction would improve agreement with the solution NMR studies. However, here we report

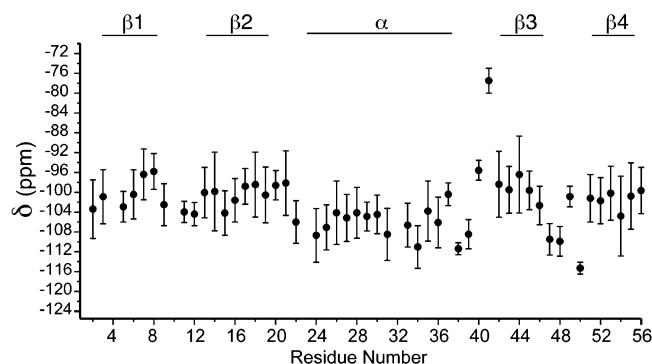


Figure 8. Plot of the anisotropy parameter, δ , versus residue number. Secondary structural elements are labeled at the top of each column. The absolute value of δ is greater in the α -helix compared to the β -sheets by an average value of 6 ppm, as discussed further within the text.

TABLE 3: Amide ^{15}N CSA Tensor Parameters Averaged by Secondary Structure

| structure ^a | δ^b |
|------------------------|----------------------|
| all ^c | -103.5 ± 5.6 ppm |
| helix ^a | -106.2 ± 2.3 ppm |
| sheet ^a | -100.5 ± 2.4 ppm |
| other ^d | -103.9 ± 3.1 ppm |

^a Secondary structure elements are presumed to be β -sheet for residues 2–8, 13–19, 43–46, and 51–55 and α -helix for residues 23–36. ^b Uncertainties quoted in this table correspond to the standard deviation within the measured values for each secondary structure element. The value for each residue is taken as the statistical average of the two measurements in cases where both N–C' and N–C α values were available. ^c G41 demonstrates a large motional averaging, as discussed in the text, and therefore is excluded from this calculation. ^d Residues in the turns, loops, or termini (9–12, 20–22, 37–40, 42, 47–50, 56).

the directly determined values from the ROCSA experiment, to avoid the propagation of error that would result from a less precise ^1H – ^{15}N dipolar coupling measurement. In our studies thus far, we have been limited by the available ^1H B_1 fields, requiring relatively slow MAS rates (~ 8 kHz) for application of the T-MREV experiment;⁹³ we anticipate that more precise effective ^1H – ^{15}N bond length measurements will be possible with new instrumentation and/or recoupling methodologies.⁹⁴

Even with relatively low precision in the previous ^1H – ^{15}N dipolar coupling measurements, some dynamic regions were evident in the GB1 backbone.⁷³ For example, in the turn connecting the α -helix to the β 3-strand of GB1, G41 shows $\sim 25\%$ scaling of ^1H – ^{15}N coupling relative to the majority of the backbone sites. Likewise, their ^{15}N CSA tensors are significantly smaller in magnitude than the average for the rest of the protein. Specifically G41 has an anisotropy parameter of -74.8 ± 2.9 ppm (from the N–C' experiment) or -81.2 ± 3.4 ppm (from the N–C α experiment); the difference between the two measurements for this residue may arise from the orientation dependence of the ^{15}N – ^{13}C dipolar transfer and/or asymmetric averaging of the tensors due to dynamics. Nevertheless, clearly the magnitude of the tensor observed at this residue is $\sim 25\%$ less than the bulk, and the neighboring sites (D40, E42) are also smaller than the average values although the difference is less pronounced; therefore in calculating the average tensor magnitude over the entire protein, we have excluded these values. If these residues are removed from the calculation of average tensor magnitude for the entire protein, we find average values of $\delta = -103.5$ ppm. This correction brings our values into slightly better agreement with those reported by solution NMR studies, but a significant discrepancy still exists. We did

not perform quantitative dynamic averaging corrections, reserving this for a future study in which the orientation dependence will also be addressed in greater detail.

Not all turns exhibit scaling of the tensor magnitude due to dynamics. In fact, the single largest tensor observed in our study is that of K50, a residue in the turn between β 3 and β 4. The value of δ for K50 is -115.1 ± 1.7 ppm as determined by the N–C' experiment; this is the highest precision fit in our entire study. Likewise the value from the N–C α experiment fits to $\delta = -116.1 \pm 3.4$ ppm, the largest anisotropy observed in the entire study. When these two results are combined statistically, we find an average value of $\delta = -115.3 \pm 1.6$ ppm. This result is significantly greater than the next largest ^{15}N tensors in GB1 (G38 and A34) by ~ 4 ppm; the average δ for G38 is -111.4 ± 1.6 ppm and for A34 is -111.0 ± 2.9 ppm. The observation of an unusually large ^{15}N CSA tensor for K50 is interesting, especially considering our previous observation of a large $^{13}\text{C}\alpha$ tensor for this residue.⁷⁴ These large tensor values likely are a consequence of the fact that K50 has an unusual value of $+58^\circ$ for the ϕ backbone torsion angle (in the orthorhombic crystal structure, PDB code 1PGA).⁹⁵ This conformation creates an unusual situation in which the amide and α protons are eclipsed, and nearby heavy atoms have a large amount of steric interaction within the tight turn geometry. As ϕ decreases from $+58^\circ$, this deshielding effect is systematically increased (i.e., the anisotropy parameter decreases). For example, K28 is found in the helix ($\phi = -69^\circ$) and has $\delta = -104.1 \pm 3.2$ ppm, and K13 is found in the β 2 strand ($\phi = -138^\circ$) and has $\delta = -100.1 \pm 3.2$ ppm. This trend in tensor magnitude follows the average behavior as noted above according to secondary structure, but K50 represents the extreme case.

This trend is observed also among other residue types in GB1 that are found in a variety of backbone geometries, including Gly, Thr, and Ala. As noted above, G41 is motionally averaged, and therefore we omit it from further discussion. However, the remaining Gly residues illustrate the trend well. G38, with a positive ϕ value ($+77^\circ$), has the largest δ of -111.4 ± 1.6 ppm (weighted average value). G9, located in a turn with a near-helical ϕ value of -92° , has $\delta = -102.5 \pm 2.9$ ppm. G14, within β 2 ($\phi = +169^\circ$), has $\delta = -99.8 \pm 4.0$ ppm. Therefore within the Gly residues, again the trend is observed that the ^{15}N tensor magnitude decreases as the ϕ value approaches trans geometry for C'[i]–N[i]–C α [i]–C'[i]. The tensor magnitudes vary by more than 10%, which is well beyond the range of statistical uncertainty in the data.

Among the Thr residues, most are in β -sheet (T16, T17, T18, T44, T51, T53, T55) or β -turn (T11, T49) geometries and have δ values near -100 ppm, ranging from a low of -96 ppm for T44 to a high of -104 ppm for T11, in a turn connecting β 1 and β 2. The mean \pm standard deviation of those β -conformation Thr residues is -100.2 ± 2.3 ppm. The only Thr in a helical conformation, T25, demonstrates a somewhat larger anisotropy parameter, -107.1 ± 3.0 ppm. Likewise, Ala residues follow the trend but emphasize the opposite preponderance of secondary structure type; the majority of Ala residues are in the helix (A23, A24, A26, A34) or in helical turn geometry (A48). These ^{15}N tensors range (in their weighted averages) from -104.1 ppm (A26) to -110.9 ppm (A48), with an average of -108.4 ± 3.0 ppm, whereas the only Ala residue in a β -turn conformation (A20) has a much smaller value of -98.6 ± 3.0 ppm. This trend appears in other residue types as well, indicating that the effect is dominated by secondary, not primary, structure.

Conclusions

We have presented a systematic study of the majority of ¹⁵N amide CSA tensors in a microcrystalline protein of known structure. The ¹⁵N and ¹³C spectra of GB1 have exceptionally good sensitivity and resolution, which enabled a site-specific analysis at the majority of amide resonances in the protein with high accuracy and precision. The absolute magnitudes of tensor measurements were validated by comparison to model compounds as well as to the traditional Herzfeld–Berger method of analysis, in the small number of sites in GB1 where the ¹⁵N signals were resolved in 1D CP-MAS spectra. Consistency within our experiments was further demonstrated by performing two types of 3D ROCSA experiments, in which different polarization transfer pathways were employed. This resulted in complementary sets of resolved peaks to increase the total number of sites reported but also a large number of cases in which both N–C′- and N–Cα-based experiments could be directly compared. The data sets were identical within their respective statistical errors, and the combined data yielded higher precision fits of the fundamental CSA parameters. The key to identifying systematic trends in our study was the ability to measure several dozen tensor line shapes in the same experiment. This strategy avoided the potential for systematic errors inherent to performing a series of 1D or 2D experiments on site-specifically labeled samples; for example, sample-to-sample variations in local conformation, instrumental fluctuations, calibration errors, and the radio frequency profile of the sample region (a function of sample packing geometry) might all cause variations in the resulting line shapes. By comparison of data from the same 3D data set, many of the practical origins for line shape variations are avoided.

The ability to compare line shapes directly throughout the entire protein within the same data sets acquired from the same experiments enabled the most complete analysis of ¹⁵N tensors in a solid protein to date and helped us to quantify significant trends as a function of secondary structure. Although similar effects have been observed previously by solution NMR studies, in our results the amplitude of this difference is greater. Specifically, ¹⁵N tensors of helical residues are systematically almost 6% larger in magnitude than β-sheet residues. This trend is amplified further within amino acid residue types that are present both in α and β conformations. Extreme examples of this effect are observed in residues with positive ϕ values, K50 and G38. To our knowledge, this correlation has not previously been observed.

This study represents an important first step toward development of improved computation and semiempirical analysis of ¹⁵N CSAs in proteins. Our measurements have been performed in a protein whose high-resolution X-ray and solution NMR structures are known and for which previous and continuing studies by SSNMR are available. This body of data will enable an especially thorough and accurate computational analysis of ¹⁵N tensors in future studies. The examples of specific residues demonstrating unusual tensor parameters in GB1 will serve as benchmarks for validating computational models that take into account not only primary and secondary structure but also local electrostatics, side-chain conformation, and hydrogen bonding.

Acknowledgment. This material is based upon work supported by the National Science Foundation under Grant No. 0347824 (CAREER Award to C.M.R.). The authors thank Professor Eric Oldfield for stimulating discussions, Dr. Paul Molitor and Benjamin Fisher (VOICE NMR Facility) for technical assistance, John M. Boettcher for preparing the GB1

sample, and Professor Malcolm H. Levitt (University of Southampton, U. K.) for providing the Mathematica packages for Herzfeld–Berger sideband analysis.

Supporting Information Available: Larger version of CP-MAS 1D ¹⁵N spectra of GB1 used for Herzfeld–Berger analysis and experimental and simulated sideband intensity values for the sites discussed in the text. This material is available free of charge via the Internet at <http://pubs.acs.org>.

References and Notes

- (1) Gutowsky, H. S. *Annu. Rev. Phys. Chem.* **1954**, *5*, 333.
- (2) Oldfield, E. *Annu. Rev. Phys. Chem.* **2002**, *53*, 349–378.
- (3) Oldfield, E. *J. Biomol. NMR* **1995**, *5*, 217–225.
- (4) Paul, E. G.; Grant, D. M. *J. Am. Chem. Soc.* **1963**, *85*, 1701–1702.
- (5) Saito, H.; Tabeta, R.; Sjöhi, A.; Ozaki, T.; Ando, I. *Macromolecules* **1983**, *16*, 1050–1057.
- (6) Saito, H.; Tabeta, R. *Chem. Lett.* **1985**, *1*, 83–86.
- (7) Saito, H. *Magn. Reson. Chem.* **1986**, *24*, 835–852.
- (8) Ando, I.; Saito, H.; Tabeta, R.; Shoji, A.; Ozaki, T. *Macromolecules* **1984**, *17*, 457–461.
- (9) Spera, S.; Bax, A. *J. Am. Chem. Soc.* **1991**, *113*, 5490–5492.
- (10) Wishart, D. S.; Sykes, B. D.; Richards, F. M. *Biochemistry* **1992**, *31*, 1647–1651.
- (11) Wishart, D. S.; Sykes, B. D. *J. Biomol. NMR* **1994**, *4*, 171–180.
- (12) Cornilescu, G.; Delaglio, F.; Bax, A. *J. Biomol. NMR* **1999**, *13*, 289–302.
- (13) Luca, S.; Filippov, D. V.; van Boom, J. H.; Oschkinat, H.; de Groot, H. J. M.; Baldus, M. *J. Biomol. NMR* **2001**, *20*, 325–331.
- (14) Laws, D. D.; de Dios, A. C.; Oldfield, E. *J. Biomol. NMR* **1993**, *3*, 607–612.
- (15) Wishart, D. S.; Watson, M. S.; Boyko, R. F.; Sykes, B. D. *J. Biomol. NMR* **1997**, *10*, 329–336.
- (16) Wishart, D. S.; Nip, A. M. *Biochem. Cell Biol.* **1998**, *76*, 153–163.
- (17) Witter, R.; Priess, W.; Sternberg, U. *J. Comput. Chem.* **2002**, *23*, 298–305.
- (18) Sternberg, U.; Witter, R.; Ulrich, A. S. *Annu. Rep. NMR Spectrosc.* **2004**, *52*, 53–104.
- (19) Neal, S.; Nip, A. M.; Zhang, H. Y.; Wishart, D. S. *J. Biomol. NMR* **2003**, *26*, 215–240.
- (20) Zhang, H. Y.; Neal, S.; Wishart, D. S. *J. Biomol. NMR* **2003**, *25*, 173–195.
- (21) Wishart, D. *Curr. Pharm. Biotechnol.* **2005**, *6*, 105–120.
- (22) Xu, X. P.; Case, D. A. *J. Biomol. NMR* **2001**, *21*, 321–333.
- (23) Wang, Y. J.; Wishart, D. S. *J. Biomol. NMR* **2005**, *31*, 143–148.
- (24) Case, D. A. *Curr. Opin. Struct. Biol.* **1998**, *8*, 624–630.
- (25) Sitkoff, D.; Case, D. A. *Prog. Nucl. Magn. Reson. Spectrosc.* **1998**, *32*, 165–190.
- (26) Poon, A.; Birn, J.; Ramamoorthy, A. *J. Phys. Chem. B* **2004**, *108*, 16577–16585.
- (27) Le, H. B.; Oldfield, E. *J. Phys. Chem.* **1996**, *100*, 16423–16428.
- (28) de Dios, A. C.; Oldfield, E. *Solid State Nucl. Magn. Reson.* **1996**, *6*, 101–125.
- (29) Brender, J. R.; Taylor, D. M.; Ramamoorthy, A. *J. Am. Chem. Soc.* **2001**, *123*, 914–922.
- (30) Bodenhausen, G.; Ruben, J. *Chem. Phys. Lett.* **1980**, *69*, 185–189.
- (31) Morris, G. A.; Freeman, R. *J. Am. Chem. Soc.* **1979**, *101*, 760–762.
- (32) Muller, L. *J. Am. Chem. Soc.* **1979**, *101*, 4481–4484.
- (33) Pervushin, K.; Riek, R.; Wider, G.; Wuthrich, K. *Proc. Natl. Acad. Sci. U.S.A.* **1997**, *94*, 12366–12371.
- (34) Pervushin, K.; Riek, R.; Wider, G.; Wuthrich, K. *J. Am. Chem. Soc.* **1998**, *120*, 6394–6400.
- (35) Rance, M.; Loria, J. P.; Palmer, A. G. *J. Magn. Reson.* **1999**, *136*, 92–101.
- (36) Shuker, S. B.; Hajduk, P. J.; Meadows, R. P.; Fesik, S. W. *Science* **1996**, *274*, 1531–1534.
- (37) Olejniczak, E. T.; Meadows, R. P.; Wang, H.; Cai, M. L.; Nettekheim, D. G.; Fesik, S. W. *J. Am. Chem. Soc.* **1999**, *121*, 9249–9250.
- (38) Kroenke, C. D.; Loria, J. P.; Lee, L. K.; Rance, M.; Palmer, A. G. *J. Am. Chem. Soc.* **1998**, *120*, 7905–7915.
- (39) Vugmeyster, L.; Kroenke, C. D.; Picart, F.; Palmer, A. G.; Raleigh, D. P. *J. Am. Chem. Soc.* **2000**, *122*, 5387–5388.
- (40) Palmer, A. G. *Annu. Rev. Biophys. Biomol. Struct.* **2001**, *30*, 129–155.

- (41) Palmer, A. G.; Kroenke, C. D.; Loria, J. P. Nuclear magnetic resonance methods for quantifying microsecond-to-millisecond motions in biological macromolecules. *Methods Enzymol.* **2001**, *339*, 204–238.
- (42) Palmer, A. G. *Chem. Rev.* **2004**, *104*, 3623–3640.
- (43) Massi, F.; Grey, M. J.; Palmer, A. G. *Protein Sci.* **2005**, *14*, 735–742.
- (44) Ramamoorthy, A.; Opella, S. J. *Solid State Nucl. Magn. Reson.* **1995**, *4*, 387–392.
- (45) Ramamoorthy, A.; Wu, C. H.; Opella, S. J. *J. Magn. Reson.* **1999**, *140*, 131–140.
- (46) Ramamoorthy, A.; Wu, C. H.; Opella, S. J. *J. Magn. Reson. B* **1995**, *107*, 88–90.
- (47) Nevzorov, A. A.; Mesleh, M. F.; Opella, S. J. *Magn. Reson. Chem.* **2004**, *42*, 162–171.
- (48) Park, S. H.; Mrse, A. A.; Nevzorov, A. A.; Mesleh, M. F.; Oblatt-Montal, M.; Montal, M.; Opella, S. J. *J. Mol. Biol.* **2003**, *333*, 409–424.
- (49) Thiriot, D. S.; Nevzorov, A. A.; Zagayanskiy, L.; Wu, C. H.; Opella, S. J. *J. Mol. Biol.* **2004**, *341*, 869–879.
- (50) Opella, S. J.; Marassi, F. M. *Chem. Rev.* **2004**, *104*, 3587–3606.
- (51) Tjandra, N.; Szabo, A.; Bax, A. *J. Am. Chem. Soc.* **1996**, *118*, 6986–6991.
- (52) Boyd, J.; Redfield, C. *J. Am. Chem. Soc.* **1998**, *120*, 9692–9693.
- (53) Boyd, J.; Redfield, C. *J. Am. Chem. Soc.* **1999**, *121*, 7441–7442.
- (54) Damberg, P.; Jarvet, J.; Allard, P.; Graslund, A. *J. Biomol. NMR* **1999**, *15*, 27–37.
- (55) Kroenke, C. D.; Rance, M.; Palmer, A. G. *J. Am. Chem. Soc.* **1999**, *121*, 10119–10125.
- (56) Cornilescu, G.; Bax, A. *J. Am. Chem. Soc.* **2000**, *122*, 10143–10154.
- (57) Kurita, J.; Shimahara, H.; Utsunomiya-Tate, N.; Tate, S. *J. Magn. Reson.* **2003**, *163*, 163–173.
- (58) Damberg, P.; Jarvet, J.; Graslund, A. *J. Am. Chem. Soc.* **2005**, *127*, 1995–2005.
- (59) Loth, K.; Pelupessy, P.; Bodenhausen, G. *J. Am. Chem. Soc.* **2005**, *127*, 6062–6068.
- (60) Harbison, G.; Herzfeld, J.; Griffin, R. G. *J. Am. Chem. Soc.* **1981**, *103*, 4752–4754.
- (61) Harbison, G. S.; Jelinski, L. W.; Stark, R. E.; Torchia, D. A.; Herzfeld, J.; Griffin, R. G. *J. Magn. Reson.* **1984**, *60*, 79–82.
- (62) Oas, T. G.; Hartzell, C. J.; Dahlquist, F. W.; Drobny, G. *Biophys. J.* **1986**, *49*, A328.
- (63) Hartzell, C. J.; Whitfield, M.; Oas, T. G.; Drobny, G. P. *J. Am. Chem. Soc.* **1987**, *109*, 5966–5969.
- (64) Oas, T. G.; Hartzell, C. J.; Dahlquist, F. W.; Drobny, G. P. *J. Am. Chem. Soc.* **1987**, *109*, 5962–5966.
- (65) Lee, D. K.; Wittebort, R. J.; Ramamoorthy, A. *J. Am. Chem. Soc.* **1998**, *120*, 8868–8874.
- (66) Shoji, A.; Ozaki, T.; Fujito, T.; Deguchi, K.; Ando, I.; Magoshi, J. *J. Mol. Struct.* **1998**, *441*, 251–266.
- (67) Lee, D. K.; Santos, J. S.; Ramamoorthy, A. *Chem. Phys. Lett.* **1999**, *309*, 209–214.
- (68) Shekar, S. C.; Ramamoorthy, A.; Wittebort, R. J. *J. Magn. Reson.* **2002**, *155*, 257–262.
- (69) Chekmenev, E. Y.; Zhang, Q. W.; Waddell, K. W.; Mashuta, M. S.; Wittebort, R. J. *J. Am. Chem. Soc.* **2004**, *126*, 379–384.
- (70) Waddell, K. W.; Chekmenev, E. Y.; Wittebort, R. J. *J. Am. Chem. Soc.* **2005**, *127*, 9030–9035.
- (71) Herzfeld, J.; Berger, A. E. *J. Chem. Phys.* **1980**, *73*, 6021.
- (72) Hong, M.; Gross, J. D.; Hu, W.; Griffin, R. G. *J. Magn. Reson.* **1998**, *135*, 169–177.
- (73) Franks, W. T.; Zhou, D. H.; Wylie, B. J.; Money, B. G.; Graesser, D. T.; Frericks, H. L.; Sahota, G.; Rienstra, C. M. *J. Am. Chem. Soc.* **2005**, *127*, 12291–12305.
- (74) Wylie, B. J.; Franks, T.; Graesser, D. T.; Rienstra, C. M. *J. Am. Chem. Soc.* **2005**, *127*, 11946–11947.
- (75) Chan, J. C. C.; Tycko, R. *J. Am. Chem. Soc.* **2003**, *125*, 11828–11829.
- (76) Chan, J. C. C.; Tycko, R. *J. Chem. Phys.* **2003**, *118*, 8378–8389.
- (77) Baldus, M.; Petkova, A. T.; Herzfeld, J. H.; Griffin, R. G. *Mol. Phys.* **1998**, *95*, 1197–1207.
- (78) Rienstra, C. M.; Hohwy, M.; Hong, M.; Griffin, R. G. *J. Am. Chem. Soc.* **2000**, *122*, 10979–10990.
- (79) Bennett, A. E.; Rienstra, C. M.; Auger, M.; Lakshmi, K. V.; Griffin, R. G. *J. Chem. Phys.* **1995**, *103*, 6951–6958.
- (80) Delaglio, F.; Grzesiek, S.; Vuister, G. W.; Zhu, G.; Pfeifer, J.; Bax, A. *J. Biomol. NMR* **1995**, *6*, 277–293.
- (81) Haeberlen, U. *High-Resolution NMR in Solids: Selective Averaging*; Academic Press: New York, 1976.
- (82) Bak, M.; Rasmussen, J. T.; Nielsen, N. C. *J. Magn. Reson.* **2000**, *147*, 296–330.
- (83) Waugh, J. S. Average Hamiltonian Theory. In *Encyclopedia of Magnetic Resonance*; Wiley: New York, 1996; pp 849–854.
- (84) Ghose, R.; Eykyn, T. R.; Bodenhausen, G. *Mol. Phys.* **1999**, *96*, 1281–1288.
- (85) Eden, M. *Concepts Magn. Reson. A* **2003**, *17*, 117–154.
- (86) Eden, M. *Concepts Magn. Reson. A* **2003**, *18*, 1–23.
- (87) Eden, M. *Concepts Magn. Reson. A* **2003**, *18*, 24–55.
- (88) Eden, M.; Levitt, M. H. *J. Magn. Reson.* **1998**, *132*, 220–239.
- (89) Press, W. H.; Teukolsky, S. A.; Vetterling, W. T.; Flannery, B. P. *Numerical Recipes*, 2nd ed.; Cambridge University Press: Cambridge, U. K., 1992; p 963.
- (90) Dixon, W. T. *J. Chem. Phys.* **1982**, *77*, 1800–1809.
- (91) Kolbert, A. C.; Griffin, R. G. *Chem. Phys. Lett.* **1990**, *166*, 87–91.
- (92) Rienstra, C. M.; Hohwy, M.; Mueller, L. J.; Jaroniec, C. P.; Reif, B.; Griffin, R. G. *J. Am. Chem. Soc.* **2002**, *124*, 11908–11922.
- (93) Hohwy, M.; Jaroniec, C. P.; Reif, B.; Rienstra, C. M.; Griffin, R. G. *J. Am. Chem. Soc.* **2000**, *122*, 3218–3219.
- (94) Zhao, X.; Eden, M.; Levitt, M. H. *Chem. Phys. Lett.* **2001**, *342*, 353–361.
- (95) Gallagher, T.; Alexander, P.; Bryan, P.; Gilliland, G. L. *Biochemistry* **1994**, *33*, 4721–4729.